CHEMISTRY OF MATERIALS

pubs.acs.org/cm Article

Lithium Thiostannate Spinels: Air-Stable Cubic Semiconductors

Michael A. Quintero, Shiqiang Hao, Sawankumar V. Patel, Jin-Ke Bao, Xiuquan Zhou, Yan-Yan Hu, Chris Wolverton, and Mercouri G. Kanatzidis*

Cite This: *Chem. Mater.* 2021, 33, 2080−2089 Read Online

ACCESS | Metrics & More | Article Recommendations | Supporting Information

ABSTRACT: Lithium chalcogenide materials have been studied less than other alkali metal analogs and are of interest as ion conductors and semiconductors capable of thermal neutron detection. Herein, we describe the structural, thermal, magnetic, electronic, and ionic properties of a new family of cubic lithium thiospinels $Li_2MSn_3S_8$ (M = Mg, Fe, Mn, Ni, Co) and $Li_{1.66}CuSn_{3.33}S_8$. All compounds crystallize in the $Fd\bar{3}m$ space group and exhibit site occupancy disorder with Sn and M on the octahedral site for M = Mg, Fe, Mn, Ni, Co. The $Li_{1.66}CuSn_{3.33}S_8$ compound also exhibits occupancy disorder on the tetrahedral sites between Li and Cu, as well as on the octahedral sites between Li and Sn. We demonstrate the ability to tune the physical properties of the compounds by changing their composition. By tuning the identity of the transition metal in the structure, the optical band gaps can vary between 0.91(2) and 2.19(2) eV, and electrical resistivities between 2.8×10^3 Ω-cm and 2.2×10^7Ω-cm can be achieved. Density functional theory calculations for $Li_2MgSn_3S_8$ and $Li_{1.66}CuSn_{3.33}S_8$ suggest that both materials have indirect band gaps and significantly dispersive conduction bands. A bandwidth dispersion of 0.75 and 0.70 eV along the Γ → *M* direction in the conduction band are predicted for $Li_2MgSn_3S_8$ and $Li_{1.66}CuSn_{3.33}S_8$, respectively, with an electron effective mass of 0.49 and 0.55 m_e at the Γ point. The hole effective mass in the valence band is calculated to be 1.25 m_e at the *M* point and 0.75 m_e at the *L* point for $Li_2MgSn_3S_8$ and $Li_{1.66}CuSn_{3.33}S_8$, respectively. The ionic/electronic conductivity of each compound was determined using AC electrochemical impedance spectroscopy.

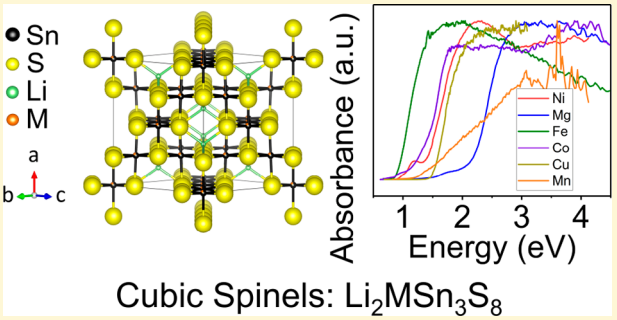

INTRODUCTION

The spinel family of compounds is well-known for both the diversity of properties observed in them and the wide range of composition that are stable in this structure type. The general formula for this family of cubic compounds is AB_2X_4, and they crystallize in the space group $Fd\bar{3}m$.[1] In this structure, the A atom is tetrahedrally coordinated by four X atoms and sits in channels created by edge-sharing BX_6 octahedra. The A and B site cations can be both transition metals and main group metals with the X anions being O^{2-}, chalcogenides,[2−5] halides,[6] as well as more complex anions, such as CN^-.[7] When X is a chalcogen (S, Se, or Te), the compounds form a subclass known as chalcospinels. These have seen growing attention as potential thermoelectric materials,[8−11] battery cathodes,[12−14] and platforms for studying aspects of condensed matter physics.[15,16] The compounds $CuTi_2S_4$,[8] $Cu_2CoTi_3S_8$,[9] $CuCr_2S_4$,[10] and ZnM_2S_4 (M = Al, Ga, In)[11] have been investigated as less toxic thermoelectric materials. $Mg_xTi_2S_4$,[12] MgM_2Q_4 (M = In, Y, Sc; Q = S, Se),[13] and $MgCr_2S_4$[14] have recently been used as promising cathode materials for Mg ion batteries. Of more fundamental interest are compounds, such as $CuIr_2S_4$,[15] which have a metal−insulator transition, $FeCr_2S_4$,[16] with an orbital glass state at low temperature, and $CuRh_2Q_4$ (Q = S, Se),[17] both of which exhibit superconductivity. The increasing variety of phenomena observed in chalcospinels thus serves as motivation to expand this family by adding new members. Furthermore, while there are several notable families of lithium chalcogenides including argyrodites,[18−20] thio-LISICONs,[21] and others[22−26] their numbers are in general, relatively limited. As such, new lithium chalcogenides could yield materials with potential for applications in special areas such as neutron detectors[27] or solid state electrolytes.[28,29]

Another motivation for studying lithium chalcogenides is to learn more about the fundamental chemistry that governs the dimensionality of metal chalcogenide frameworks in relation to their charge-balancing counterion, especially for lithium. The dimensionality of materials can be classified by the differences in bond strength in different directions.[30] The ability to predict and tune the dimensionality of continuous networks in materials has been of interest to chemists for many years. In anionic networks of a given stoichiometry charge-balanced by alkali or alkaline earth counterions, such as in the class of alkali

Received: December 4, 2020
Revised: February 2, 2021
Published: March 2, 2021

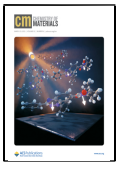

https://dx.doi.org/10.1021/acs.chemmater.0c04651
Chem. Mater. 2021, 33, 2080−2089

metal chalcogenides, a robust chemical principle has been pointed out: The smaller the size of the counterion, the higher the network dimensionality tends to be.[30−33] This has been successfully used to predict and rationalize the dimensionality of many isostoichiometric compounds of various alkali metals.[34,35] When changes in the counterion size are not sufficiently large for a given anionic framework, they may not induce a dimensional response, as seen in the AMO_2 (A = Li, Na, Rb, Cs; M = Nb, Sm, Sc) family, where their two-dimensional (2D) structure is maintained throughout substitution.[36−39] In this study, we investigated the effect of small alkali cation substitution on the dimensionality of the so-called KMS family $A_x[M_xSn_{3-x}S_6]$ (M = Mn, Mg, In etc; A= Na, K, Rb, Cs,). In this family, all known members are layered with no apparent size effect on the dimensionality of the covalent $[M_xSn_{3-x}S_6]^{x-}$ framework from Na^+ to Cs^+. For this reason, we chose to investigate the smallest alkali metal, the lithium ion, in corresponding compositions, and study its effects. We observe a striking change in the dimensionality of the framework to the three-dimensional (3D) motif of the spinel structure type.

Herein, we describe the synthesis process, crystal structure, and properties of six lithium thiostannates with the formulas $Li_{1.66}CuSn_{3.33}S_8$ and $Li_2MSn_3S_8$ (M = Mg, Fe, Mn, Ni, Co). They all exhibit 3D cubic spinel structures in contrast to the 2D structures adopted by the $A_x[M_xSn_{3-x}S_6]$ compounds.[40−42] The $Li_2MSn_3S_8$ structure (M = Mg, Fe, Mn, Ni, Co) exhibits mixed site occupancy disorder at the octahedral sites between M and Sn. $Li_{1.66}CuSn_{3.33}S_8$ also exhibits occupational disorder at the tetrahedral sites between Li and Cu as well as at the octahedral sites between Li and Sn. Across the different elements, electrical resistivities range between 2.8×10^3 for Fe and 2.2×10^7 Ω-cm for the Mg analog, and the optical band gaps range between 0.91(2) and 2.19(2) eV. Density functional theory (DFT) calculations predict that both $Li_2MgSn_3S_8$ and $Li_{1.66}CuSn_{3.33}S_8$ have indirect gaps as well as high energy dispersity in their conduction band widths with small electron carrier effective masses.

EXPERIMENTAL METHODS

The synthetic procedures for all compounds differ only in the identities and amounts used for all reagents but are otherwise identical. As such, we describe the general synthesis used to prepare both crystals and powder for each compound and provide the reagents and amounts used in the Supporting Information.

Reagents and Synthesis. All starting elements were used as obtained: Sn powder (99.999% American Elements, Los Angeles, CA), sulfur buttons S (99.99%, 5N Plus Inc., Saint-Laurent, Quebec, Canada), Li sticks (99.9% Sigma-Aldrich), Mn −325 mesh powder (99% Sigma-Aldrich), Fe powder spherical <10 μm (99.9% Alfa Aesar), Mg powder (99% Sigma-Aldrich), V powder −100 mesh (99.9% Sigma-Aldrich), Ni powder <50 μm (99.7% Sigma-Aldrich), Co powder 2 μm (99.8% Sigma-Aldrich), Cu powder −100 mesh (99% Alfa Aesar). Li_2S was prepared using condensed ammonia as reported previously.[43]

Single-Crystal Synthesis of $Li_2MSn_3S_8$ (M = Co, Mg, Fe, Mn, Ni) and $Li_{1.66}CuSn_{3.33}S_8$. Single crystals of $Li_2MgSn_3S_8$ were prepared as follows: stoichiometric amounts of Sn powder, Mg powder, S buttons, and Li_2S powder were combined in a nitrogen double glovebox and ground in an agate mortar and pestle. The powder was then added to a glassy carbon crucible and loaded into a fused silica tube with an inner diameter of 16 mm and an outer diameter of 18 mm. The tube was then evacuated to a pressure of $\sim 4 \times 10^{-3}$ mbar and flame-sealed with a tube of length ∼5 in. The sealed tube was placed into a vertical tube furnace and heated to 900 °C at a rate of 50 °C/h, soaked for 6 h, after which the furnace was turned off, and the tube was cooled to room temperature. The synthesis yielded octahedral shaped crystals for all compounds with ∼70−80% yields. For $Li_2MgSn_3S_8$ and $Li_{1.66}CuSn_{3.33}S_8$, the crystals appeared red and dark red, respectively, the color for all other compounds was black.

Phase-Pure Powder Preparation. Stoichiometric amounts of Sn powder, Mg powder, S buttons, and Li_2S powder were combined in a double glovebox filled with nitrogen and ground in an agate mortar and pestle. The homogenized powder was then loaded into a stainless-steel die and pressed into a 6 mm pellet utilizing a vise to apply the force. The pressed pellet was then placed into a glassy carbon crucible, which was then placed into a fused silica tube of outer diameter of 18 mm and inner diameter of 16 mm. Note, because glassy carbon is inert toward reactions with Li, we utilized stoichiometries in ratios identical with the target compounds, should other noninert containers be used care should be taken in adding extra Li to compensate for parasitic side reactions. The fused silica tube, containing the pellet and crucible, was evacuated to $\sim 4 \times 10^{-3}$ mbar and flame-sealed so that the final length of the tube was ∼5 in. The sealed tube was then loaded into a vertical tube furnace, such that the top of the tube was below the middle of the furnace and the tip of the thermocouple was at the same depth as the crucible. The tube was then heated to 600 °C at a rate of 50 °C/h, soaked at 600 °C for 8 h, and then cooled to room temperature by turning the furnace off. After heating, the pellet had noticeably increased to ∼2−3× in size and decreased in density. The sealed tube was then placed in a double glovebox filled with nitrogen, the tube opened, and the pellet ground in an agate mortar and pestle. The reground powder was then pressed into a 6 mm pellet and placed into the same glassy carbon crucible. The crucible was then loaded into a fused silica tube of outer diameter of 18 mm and inner diameter of 16 mm, evacuated to $\sim 4 \times 10^{-3}$ mbar, and flame-sealed. The sealed tube was then placed in a vertical tube furnace, heated to 600 °C at a rate of 100 °C, soaked at 600 °C for 8 h, after which the furnace was turned off and the tube was cooled to room temperature. For $Li_2MgSn_3S_8$, the synthesized powder was a mustard yellow color after grinding, for all other compounds the powder appeared black.

Magnetic Susceptibility. Magnetic susceptibility measurements were carried out using a magnetic property measurement system (Quantum Design MPMS). Both field-cooled (FC) and zero-field-cooled (ZFC) magnetic susceptibility measurements were made from to 1.8−300 K with an applied magnetic field of 500 Oe.

Density Functional Theory (DFT). DFT calculations were performed for the relaxed structures and total energies, within the framework of the generalized gradient approximation (GGA) of Perdew−Burke−Ernzerhof. The projector augmented wave potentials are used for the exchange correlation functional.[44] The periodic boundary conditions and plane wave basis sets are applied as implemented in the Vienna ab initio simulation package.[45] The cutoff energy was set to 500 eV for the plane wave basis set. Using a very dense k-mesh corresponding to 4000 k-points per reciprocal atom in the Brillouin zone and a small energy convergence of approximately 3 meV/cation guarantee calculation accuracy. For $Li_2MgSn_3S_8$, with experimentally determined mixed occupancy at an individual site, we first identified the lowest energy configuration from many geometrically distinct Sn/Mg configuration possibilities and then performed band structure calculations for the most favorable configuration. Simply speaking, we enumerated all structural possibilities within a 56-atom cell and ranked their electrostatic energies. For the five structures with the lowest electrostatic energies, we performed further DFT calculations to determine the most favorable (lowest energy) structure and perform band structure calculations. For structures with fully occupied single-atom sites, we did not need to perform any extra procedures related to partial occupancy. Coordinates for the optimized structures used for calculations are provided in the Supporting Information.

Electrical Conductivity and Impedance Spectroscopy. Samples were prepared for transport measurements by pressing the ground powders into pellets using a 6 mm cylindrical die and applying a force of 1 t. The pellets were placed into glassy carbon crucibles, which were then flame-sealed in an evacuated silica tube. The sealed

https://dx.doi.org/10.1021/acs.chemmater.0c04651
Chem. Mater. 2021, 33, 2080−2089

Table 1. Crystal Data and Structure Refinement Details for $Li_2MSn_3S_8$ (M = Co, Mg, Fe)

empirical formula	$Li_2CoSn_3S_8$	$Li_2MgSn_3S_8$	$Li_2FeSn_3S_8$
formula weight	685.14	650.84	682.06
temperature	293(2) K	293(2) K	293(2) K
wavelength	0.71073 Å	0.71073 Å	0.71073 Å
crystal system	cubic	cubic	cubic
space group	$Fd\bar{3}m$	$Fd\bar{3}m$	$Fd\bar{3}m$
unit cell dimensions	a = 10.4683(12) Å, α = 90°	a = 10.5720(12) Å, α = 90°	a = 10.4971(12) Å, α = 90°
	b = 10.4683(12) Å, β = 90°	b = 10.5720(12) Å, β = 90°	b = 10.4971(12) Å, β = 90°
	c = 10.4683(12) Å, γ = 90°	c = 10.5720(12) Å, γ = 90°	c = 10.4971(12) Å, γ = 90°
volume	1147.2(4) Å^3	1181.6(4) Å^3	1156.7(4) Å^3
Z	4	4	4
density (calculated)	3.968 g/cm^3	3.658 g/cm^3	3.918 g/cm^3
absorption coefficient	9.275 mm^{-1}	7.703 mm^{-1}	9.019 mm^{-1}
F(000)	1244	1184	1240
crystal size	0.2 × 0.3 × 0.2 mm^3	0.5 × 0.3 × 0.4 mm^3	0.3 × 0.2 × 0.4 mm^3
θ range for data collection	3.371−29.928°	3.338−27.365°	3.362−34.716°
index ranges	$-14 \le h \le 14$, $-14 \le k \le 14$, $-14 \le l \le 13$	$-13 \le h \le 13$, $-13 \le k \le 13$, $-13 \le l \le 13$	$-16 \le h \le 16$, $-16 \le k \le 15$, $-16 \le l \le 16$
reflections collected	2757	2282	4085
independent reflections	104 [R_{int} = 0.0878]	87 [R_{int} = 0.0571]	148 [R_{int} = 0.0351]
completeness to θ = 25.242°	98.6%	100%	98.6%
refinement method	Full-matrix least-squares on F^2	full-matrix least-squares on F^2	full-matrix least-squares on F^2
data/restraints/parameters	104/6/7	87/0/8	148/0/7
goodness-of-fit	1.129	1.456	1.305
final R indices[a] [$I > 2\sigma(I)$]	R_{obs} = 0.0358, wR_{obs} = 0.0834	R_{obs} = 0.0329, wR_{obs} = 0.0762	R_{obs} = 0.0308, wR_{obs} = 0.0791
R indices[a] [all data]	R_{all} = 0.0390, wR_{all} = 0.0870	R_{all} = 0.0396, wR_{all} = 0.0780	R_{all} = 0.0345, wR_{all} = 0.0811
extinction coefficient	N/A	0.0017(3)	N/A
largest diff. peak and hole	0.803 and −1.830 e Å^{-3}	1.170 and −0.755 e Å^{-3}	0.724 and −2.483 e Å^{-3}

[a] $R = \Sigma||F_o| - |F_c||/\Sigma|F_o|$, $wR = \{\Sigma[w(|F_o|^2 - |F_c|^2)^2]/\Sigma[w(|F_o|^4)]\}^{1/2}$, and $w = 1/[\sigma 2(F_o^2) + (0.0154P)^2 + 141.3500P]$ where $P = (F_o^2 + 2F_c^2)/3$.

tubes were annealed at 500 °C for 4 h and then cooled to room temperature before opening. Pellets for electrical conductivity measurements were prepared by applying colloidal carbon paste to each face of the pellet and attaching copper wire leads to the sides.

Ionic conductivity was determined by alternating current (AC) impedance spectroscopy using a Gamry Analyzer Reference 600+. Indium foils were pressed onto the surfaces of the pellets to serve as blocking electrodes, and the pellets were placed in a custom-built cylindrical cell. Impedance measurements were conducted at room temperature (~21 °C) over a frequency range of 5 MHz to 1 Hz with an applied voltage of 10 mV.

RESULTS AND DISCUSSION

Synthesis and Crystal Structures. Generally, solid-state reactions involve powders of starting materials, grinding them together, and heating the mixtures to high temperatures for extended periods of time to reach a pure compound, often in an iterative manner. When this reaction route does not proceed through a molten state, it becomes diffusion-limited, and as such, it is typical for reaction times to extend to several hours, or even several days.[46] The synthetic procedures used to prepare the compounds reported herein involve direct solid-state reactions but are relatively quick as all compounds can be prepared in little more than a day. We attribute this in part to the small size of Li, which allows for fast rates of diffusion even well below the melting temperature as evidenced by the existence of several solid state Li ion conductors.[47]

The differential thermal analysis (DTA) of all the chalcospinel compounds was a challenge to carry out as the measurements show thermal events near 800 °C with several other thermal events occurring at lower temperatures (see Supporting Information for DTA of $Li_2MnSn_3S_8$). These events most likely correspond to reactions of the starting materials with the protective carbon coating[48] on the inner surface of the fused silica ampules in addition to with the silica itself as evidenced by glass attack after heating. In one instance, these side reactions resulted in the explosion of an ampule during measurement, which severely damaged an outer crucible used to hold the ampule requiring replacement. As such thorough characterization of the thermal behavior of all compounds was forgone as the quality of the carbon coatings in the inner surfaces of the silica ampules used for measurement was too inconsistent to ensure the safety of the equipment. This parasitic reaction removes lithium from the material, resulting in the formation of at least one or more secondary phases that have yet to be identified. In fact, the lithium thiospinel compounds most likely melt congruently, as shown by heating phase-pure material until molten in glassy carbon crucibles (that have been flame-sealed in vacuum), whereupon the same phase is fully recovered on cooling with no secondary phases.

All the compounds crystallize in the spinel structure with the cubic space group $Fd\bar{3}m$, with the general formula AB_2S_4, (see Tables 1 and 2). The compounds have the general formulas $Li_{2-x}MSn_3S_8$ (M = Mg, Fe, Mn, Ni, Co) or $Li_{1.66}CuSn_{3.33}S_8$. Energy-dispersive X-ray spectroscopy (EDS) data (see Supporting Information) show approximate agreement with our crystallographically refined compositions. Their structure can be described as a face-centered cubic (FCC) lattice of S anions, where the B cations are octahedrally coordinated by S anions occupying half of the octahedral sites, see Figure 1e, and the A cations are tetrahedrally coordinated by S anions occupying an eighth of the tetrahedral sites,[1] see Figure 1f. The

https://dx.doi.org/10.1021/acs.chemmater.0c04651
Chem. Mater. 2021, 33, 2080−2089

Table 2. Crystal Data and Structure Refinement Details for $Li_{1.66}CuSn_{3.33}S_8$ and $Li_2MSn_3S_8$ (M = Mn, Ni)

empirical formula	$CuLi_{1.67}Sn_{3.33}S_8$	$Li_2MnSn_3S_8$	$Li_2NiSn_3S_8$
formula weight	726.62	681.15	684.59
temperature	293(2) K	293(2) K	300.15 K
wavelength	0.71073 Å	0.71073 Å	0.71073 Å
crystal system	cubic	cubic	cubic
space group	$Fd\bar{3}m$	$Fd\bar{3}m$	$Fd\bar{3}m$
unit cell dimensions	a = 10.4920(12) Å, α = 90°	a = 10.5233(12) Å, α = 90°	a = 10.4750(12) Å, α = 90°
	b = 10.4920(12) Å, β = 90°	b = 10.5233(12) Å, β = 90°	b = 10.4750(12) Å, β = 90°
	c = 10.4920(12) Å, γ = 90°	c = 10.5233(12) Å, γ = 90°	c = 10.4750(12) Å, γ = 90°
volume	1155.0(4) Å^3	1183.9(4) Å^3	1149.4(4) Å^3
Z	4	4	4
density (calculated)	4.180 g/cm^3	3.823 g/cm^3	3.959 g/cm^3
Absorption coefficient	10.316 mm^{-1}	8.791 mm^{-1}	9.452 mm^{-1}
F(000)	1314	1236	1248
crystal size	0.5 × 0.5 × 0.3 mm^3	0.4 × 0.3 × 0.4 mm^3	0.3 × 0.4 × 0.5 mm^3
θ range for data collection	3.363−28.931°	3.353−28.837°	3.369−29.907°
index ranges	$-14 \le h \le 14$, $-14 \le k \le 14$, $-14 \le l \le 14$	$-14 \le h \le 14$, $-12 \le k \le 14$, $-14 \le l \le 14$	$-14 \le h \le 11$, $-14 \le k \le 14$, $-14 \le l \le 14$
reflections collected	2560	2605	3471
independent reflections	95 [R_{int} = 0.0209]	98 [R_{int} = 0.0909]	104 [R_{int} = 0.0422]
completeness to θ = 25.242°	95.7%	100%	98.6%
refinement method	full-matrix least-squares on F^2	full-matrix least-squares on F^2	full-matrix least-squares on F^2
data/restraints/parameters	95/0/8	98/0/7	104/0/7
goodness-of-fit	1.153	1.192	1.243
final R indices[a] [$I > 2\sigma(I)$]	R_{obs} = 0.0430, wR_{obs} = 0.0942	R_{obs} = 0.0463, wR_{obs} = 0.1198	R_{obs} = 0.0487, wR_{obs} = 0.1085
R indices[a] [all data]	R_{all} = 0.0441, wR_{all} = 0.0949	R_{all} = 0.0481, wR_{all} = 0.1220	R_{all} = 0.0494, wR_{all} = 0.1089
extinction coefficient	N/A	N/A	N/A
largest diff. peak and hole	3.089 and −2.197 e Å^{-3}	1.086 and −2.483 e Å^{-3}	6.177 and −0.982 e Å^{-3}

[a] $R = \Sigma||F_o| - |F_c||/\Sigma|F_o|$, $wR = \{\Sigma[w(|F_o|^2 - |F_c|^2)^2]/\Sigma[w(|F_o|^4)]\}^{1/2}$ and $w = 1/[\sigma^2(F_o^2) + (0.0154P)^2 + 141.3500P]$ where $P = (F_o^2 + 2F_c^2)/3$.

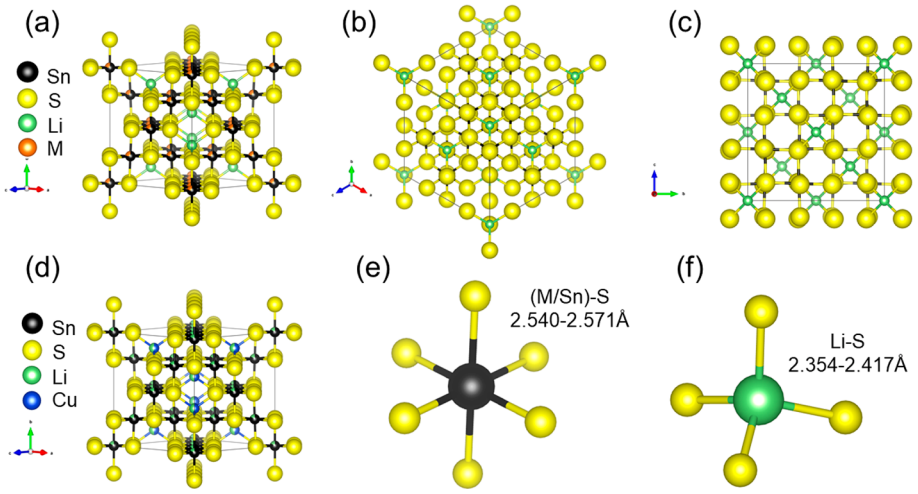

Figure 1. Crystal structure viewed along the (a) [110], (b) [111], and (c) [001] directions of $Li_{2-x}MSn_3S_8$ (M = Mg, Fe, Mn, Ni, Co) and the (d) [110] direction of $Li_{1.66}CuSn_{3.33}S_8$. Local coordination of (e) M/Sn atoms to sulfur and (f) lithium to sulfur.

Table 3. Selected Bond Lengths for $Li_{2-x}MSn_3S_8$ (M = Mg, Fe, Mn, Ni, Co; x = 0,1) and $Li_{1.66}CuSn_{3.33}S_8$

bond	$Li_2FeSn_3S_8$	$Li_2CoSn_3S_8$	$Li_2MnSn_3S_8$	$Li_2NiSn_3S_8$	$Li_2MgSn_3S_8$	$Li_{1.66}CuSn_{3.33}S_8$
Sn/M−S (Å)	2.5487(9)	2.545(1)	2.567(2)	2.548(2)	2.571(2)	2.566(2)
Li−S (Å)	2.407(2)	2.395(2)	2.393(3)	2.393(3)	2.417(4)	2.373(3)

Li occupies the A site with Li−S bond lengths ranging from 2.373(3) to 2.407(2) Å, as shown in Table 1. In compounds where M = Mg, Fe, Mn, Ni, and Co, Sn and M occupy the same B sites and are present in a 3:1 ratio, as shown in Figure 1a−c. In the Cu analogue, site occupancy disorder is observed at both the A and B sites, with Li and Cu having a ratio of 1:1 on the A sites and Li and Sn having a ratio of ∼1:5 on the B sites, as shown in Figure 1d.

The (Sn/M)−S bond lengths for all compounds were between 2.540(1) and 2.571(2) Å, see Table 3, which is close

https://dx.doi.org/10.1021/acs.chemmater.0c04651
Chem. Mater. 2021, 33, 2080−2089

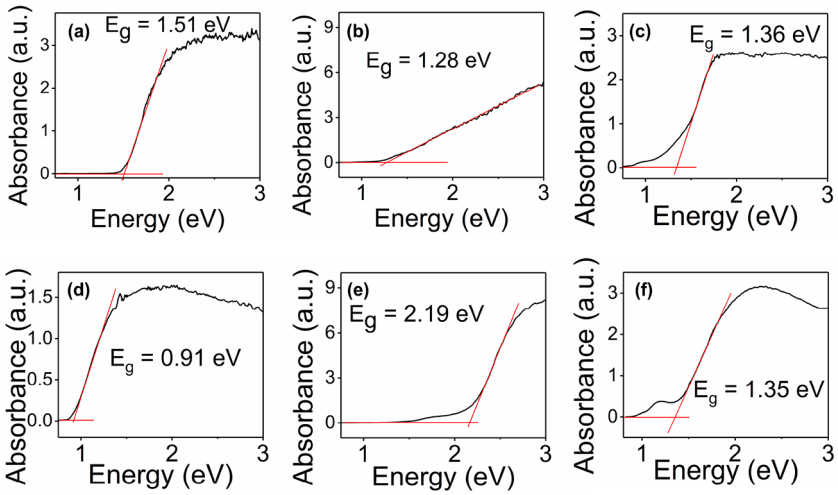

Figure 2. UV−vis absorbance spectra (derived via Kubelka−Munk equation, $F(R) = (1 - R)^2/2R$, from diffuse reflectance measurements) of (a) $Li_{1.66}CuSn_3S_8$, (b) $Li_2MnSn_3S_8$, (c) $Li_2CoSn_3S_8$, (d) $Li_2FeSn_3S_8$, (e) $Li_2MgSn_3S_8$, and (f) $Li_2NiSn_3S_8$. Red lines are included to show the baseline and linear extrapolation used to determine the band gap.

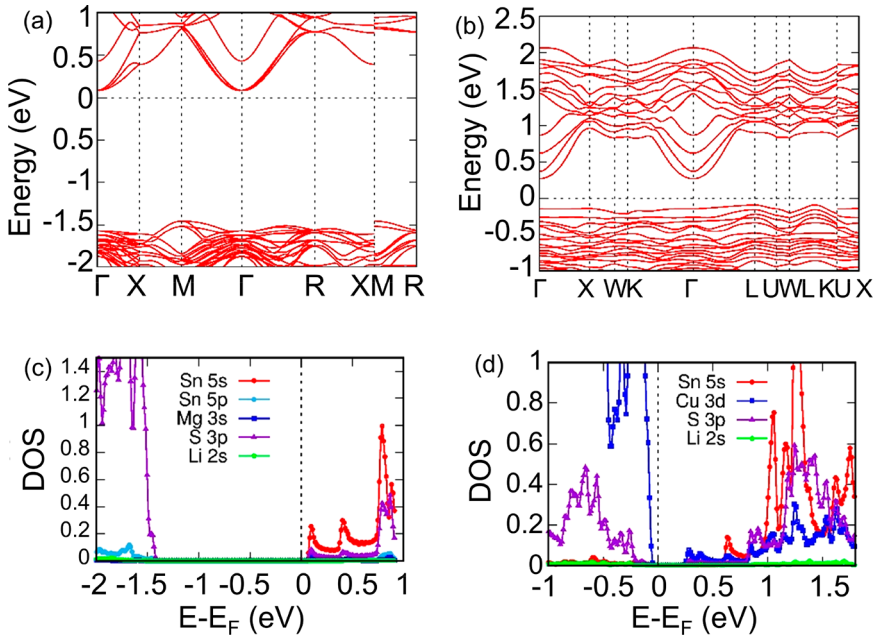

Figure 3. Electronic band structure of (a) $Li_2MgSn_3S_8$ and (b) $Li_{1.66}CuSn_3S_8$ with calculated PDOS (c and d), respectively.

to the Sn−S bond length in SnS_2 of 2.56(2) Å.[49] When the lattice parameters of the title thiospinel compounds were compared to those for $Cu_2MSn_3S_8$ (M = Mn, Fe, Co, Ni), we observe that they were larger by 0.1966 Å for Ni and 0.1073 Å for Mn.[50] Although tetrahedrally coordinated Li^+ has nearly the same ionic radius, 0.590 Å, as Cu^+, 0.60 Å,[51] the difference in size can be attributed to the covalent Cu−S bond being shorter/stronger than the ionic Li−S bond. The silver analogs, $Ag_2MSn_3S_8$ (M = Fe, Mn), have larger unit cells than the Li compounds at 10.6984 for Fe and 10.5723 Å for Mn, which is consistent with the much larger size of Ag^+ (1.00 Å) compared to Li^+.[52,53]

The chemical stability of the compounds under ambient laboratory conditions and in direct contact with H_2O is excellent over a period of several weeks, showing no observable changes in their powder X-ray diffraction patterns. More surprising is that powders submerged in water for ∼12 h and then reanalyzed via powder X-ray diffraction (PXRD) showed no change. This is a remarkable result as lithium chalcogenides are generally quite moisture-sensitive[54−56] mainly because of the strong hydration of lithium ions. The exceptional stability observed here is due to the fact that the lithium ions are well protected from hydration by the 3D spinel structure.

The fact that the layered structure of the $A_x[M_xSn_{3-x}S_6]$ (M = Mg, Mn)[40] KMS compounds is not observed when A = Li can be rationalized by the so-called counterion effect. This effect has been well documented in the study of metal polychalcogenide salts and states that an increase in the dimensionality of an anionic framework occurs when the size of the counter-cations becomes small enough for it to happen.[57] The KMS family adopts an intercalated CdI_2-type structure with SnS_2-type $[M_xSn_{3-x}S_6]$ layers of edge-sharing $(Sn/M)S_6^{2-}$ octahedral, which is charge-balanced by A^+ cations. Our results show that lithium analogs of these

https://dx.doi.org/10.1021/acs.chemmater.0c04651
Chem. Mater. 2021, 33, 2080−2089

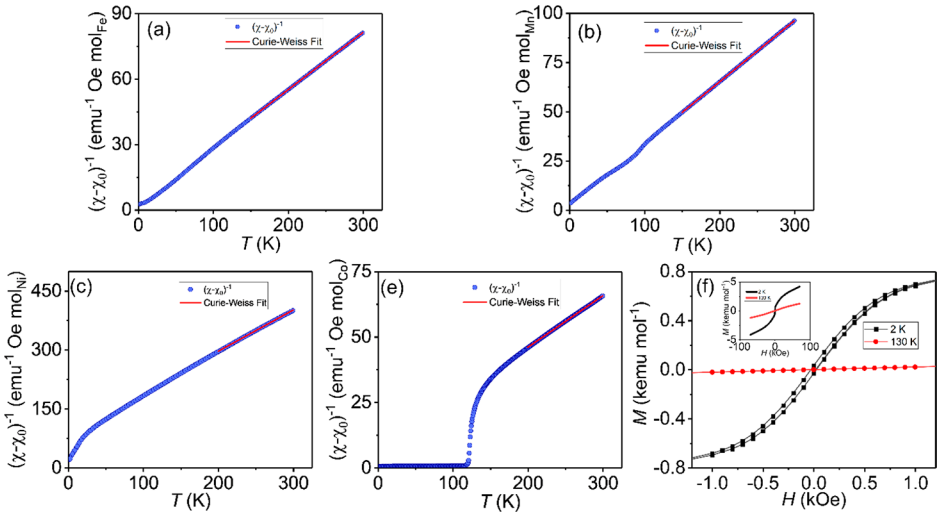

Figure 4. Inverse susceptibility with Curie–Weiss fit of (a) $Li_2FeSn_3S_8$, (b) $Li_2MnSn_3S_8$, (c) $Li_2NiSn_3S_8$, and (e) $Li_2CoSn_3S_8$. (f) Field-dependent magnetization of $Li_2CoSn_3S_8$ (inset shows full measured range).

materials adopt spinel structures as the most stable form described above. This 2D to 3D transition can be understood as a chemical pressure exerted on the layered framework when Li is used, which forces the structure to seek a smaller overall volume, thus causing linking across the third direction.[58,59] In the present system, as the ionic radius of Li^+ (0.76 Å) is smaller than that of Na^+, 1.02 Å, and K^+, 1.38 Å, it can bring the $[MSn_2S_6]$ layers closer together. If this chemical pressure causes the $[MSn_2S_6]$ layers to come too close to each other, this could result in the adoption of a more stable arrangement with a smaller overall volume, as would be expected in a 3D structure. Altogether, this implies that lower-dimensional structures containing alkali metal atoms have the potential to be converted to higher-dimensional structures via substitution of smaller alkali metals for larger ones. The M atoms on the other hand are observed to have no effect in determining the dimensionality as these are an integral part of the covalent chalcogenide framework.

Optical Properties and Electronic Structure Calculations. The materials show behavior typical of semiconductors, and the band gaps of $Li_2MgSn_3S_8$, $Li_{1.66}CuSn_{3.33}S_8$, $Li_2MnSn_3S_8$, $Li_2CoSn_3S_8$, $Li_2FeSn_3S_8$, and $Li_2NiSn_3S_8$ were measured using UV–vis diffuse reflectance spectroscopy, see Figure 2a–f. The observed band gaps are 2.19(2), 1.50(2), 1.28(2), 1.36(2), 0.91(2), and 1.35(2) eV, respectively. We can explain the large band gap of $Li_2MgSn_3S_8$ relative to the other analogs based on the fact that Mg is less electronegative than Fe, Cu, Mn, Co, and Ni, which makes the Mg–S bond more ionic in nature than the other metal–S bonds. This increased ionicity results in larger energy differences between filled S^{2-}-based orbitals in the valence bands and empty Mg^{2+} s and p orbitals in the conduction bands. The small band gap of $Li_2FeSn_3S_8$ can be explained by observing that the electronegativity of Fe is much closer to that of elemental S than those of Mg and V, and comparable to that of Cu, Mn, and Co. This larger electronegativity, in turn, makes the Fe–S bond more covalent in nature than the Mg–S bond. The higher covalency in this bond leads to smaller energy differences between the filled S^{2-} orbitals in the valence band and the empty Fe^{2+} orbitals in the conduction band.

The calculated band structures seen in Figure 3a–d predict indirect band gaps for both the Mg and Cu compounds with the valence band maxima occurring at the *M* point for $Li_2MgSn_3S_8$ and the *L* point for $Li_{1.66}CuSn_{3.33}S_8$ and the conduction band minima occurring at the Γ point for both. The calculations predict band gaps of ∼1.50 and ∼0.35 eV for these compounds, respectively, as shown in Figure 3. These numbers are far lower than the experimental values of 2.40(2) and 1.50(2) eV, respectively, owing to the well-known difficulty of accurately estimating band gaps using DFT.[60]

Although the valence to conduction band electronic transitions are predicted to be indirect, the experimental absorption edges for both compounds appear relatively sharp. The sharp increase in the absorption edge can be rationalized by the presence of direct band gap transitions at the Γ point within a very small energy interval from the proper indirect bandgap. In $Li_2MgSn_3S_8$, for example, the energy difference in the valence band between the Γ and *M* point is <0.1 eV, whereas in $Li_{1.66}CuSn_{3.33}S_8$, the energy difference between the Γ point and the *L* point is even lower at <0.05 eV. The small energy differences between the direct and indirect transitions in each compound imply that the sharpness of the experimental absorption edges is likely due to the observation of direct Γ → Γ transitions in both compounds. In fact, these small energy differences suggested by the DFT calculation results (typically done at 0 K) essentially diminish near room temperature owing to thermally induced band broadening.

The energy dispersity in the conduction band for $Li_2MgSn_3S_8$ is considerable, being ∼0.75 eV along the Γ → *M* direction, ∼0.75 eV along the Γ → *R*, and ∼0.4 eV along Γ → *X*. Similarly, $Li_{1.66}CuSn_{3.33}S_8$ exhibits high dispersity around its Γ point, though it is lower than that observed in $Li_2MgSn_3S_8$; the dispersity in the Γ → *K* and Γ → *L* directions are both ∼0.6 eV with the dispersity in the Γ → *X* direction being ∼0.7 eV. The broad conduction band widths of both compounds are reflected by the small calculated electron effective masses in each compound, with $Li_2MgSn_3S_8$ having a value of 0.49 m_e and $Li_{1.66}CuSn_{3.33}S_8$ of 0.55 m_e. The predicted hole effective masses, however, are heavier at 1.25. and 1.75 m_e, respectively, because of the lower bandwidth dispersity in their valence bands.

Magnetic Susceptibility. $Li_2FeSn_3S_8$, $Li_2MnSn_3S_8$, and $Li_2NiSn_3S_8$ exhibit Curie–Weiss behavior at $T > 120$ K as determined by temperature-dependent magnetic susceptibility

https://dx.doi.org/10.1021/acs.chemmater.0c04651
Chem. Mater. 2021, 33, 2080–2089

Table 4. Modified Curie–Weiss Fit Parameters for $Li_2MSn_3S_8$ (M = Fe, Co, Mn, Ni)

	$Li_2FeSn_3S_8$	$Li_2CoSn_3S_8$	$Li_2MnSn_3S_8$	$Li_2NiSn_3S_8$
C (emu K mol^{-1} Oe^{1-})	3.8098(3)	1.871(2)	3.2120(4)	0.9519(8)
p_{eff} (μ_B)	5.5207(2)	3.871(2)	5.0691(9)	2.760(3)
θ_W (K)	−9.732(2)	3.868(7)	−9.05(3)	−90.7(4)
χ_0 (emu mol^{-1} Oe^{1-})	0.0000245	0.000946	0.0005	0.00001

Table 5. DC Electrical Resistivities and Room Temperature Li-Ion Conductivities for $Li_{2-x}MSn_3S_8$ (M = Mg, Fe, Mn, Ni, Co) and $Li_{1.66}CuSn_{3.33}S_8$

	$Li_2FeSn_3S_8$	$Li_2CoSn_3S_8$	$Li_2MnSn_3S_8$	$Li_2NiSn_3S_8$	$Li_2MgSn_3S_8$	$Li_{1.66}CuSn_{3.33}S_8$
Ω (cm)	2.8×10^3	1.65×10^4	3.47×10^6	7.48×10^6	2.19×10^7	1.06×10^6
mS (cm^{-1})	1.9×10^{-1}	1.11	1.94×10^{-4}	1.93×10^{-3}	1.26×10^{-4}	2.55×10^{-6}

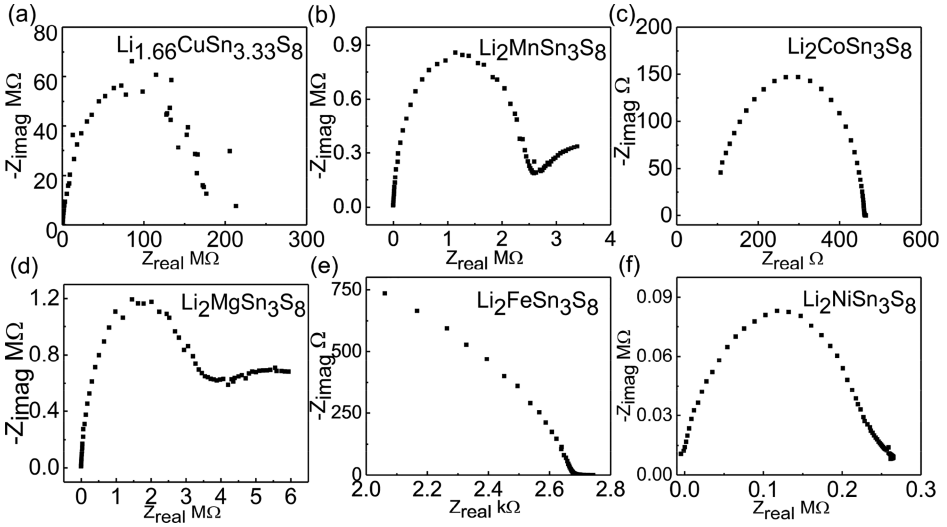

Figure 5. Room-temperature AC electrochemical impedance spectra of sintered pellets of (a) $Li_{1.66}CuSn_{3.33}S_8$, (b) $Li_2MnSn_3S_8$, (c) $Li_2CoSn_3S_8$, (d) $Li_2MgSn_3S_8$, (e) $Li_2FeSn_3S_8$, and (f) $Li_2NiSn_3S_8$.

measurements, as shown in Figure 4a–c. By fitting the temperature-dependent susceptibility data to the Curie–Weiss law, we see that both $Li_2FeSn_3S_8$ and $Li_2MnSn_3S_8$ have small negative Weiss temperatures of approximately −9.732(2) and −9.05(3) K, implying weak antiferromagnetic interactions as $\theta < 0$ (Table 4). The Curie constants for $Li_2FeSn_3S_8$ and $Li_2MnSn_3S_8$ are 3.8098(3) emu K mol^{-1} Oe^{1-} and 3.2120(4) emu K mol^{-1} Oe^{1-}, respectively. The effective magnetic moments per ion, $p_{eff} = \sqrt{8C}$, for $Li_2FeSn_3S_8$ and $Li_2MnSn_3S_8$ are 5.5207(2) and 5.0691(9) μ_B, respectively. These values are close to the expected values for Fe^{2+} and Mn^{3+} of 4.9 and 4.9 μ_B,[61] respectively. The proximity of the effective magnetic moment for $Li_2MnSn_3S_8$ to that expected for Mn^{3+} suggests that some oxidation of the material may occur, as has been observed in the KMS-1 compounds,[41] but further studies are required to confirm this. The kink in the inverse susceptibility of $Li_2MnSn_3S_8$ is attributed to a small ferromagnetic impurity, likely Mn_3O_4 with T_c = 49 K.[62] The Weiss temperature of $Li_2NiSn_3S_8$, −90.7(4) K, is larger than that in the Mn and Fe analogues, indicating stronger antiferromagnetic interactions. The Curie constant and p_{eff} for $Li_2NiSn_3S_8$ are 0.9519(8) emu K mol^{-1} Oe^{1-} and 2.760(3)μ_B, respectively. The value of the effective magnetic moment for $Li_2NiSn_3S_8$ is close to the theoretical value for Ni^{2+} of 2.83 μ_B.[61]

$Li_2CoSn_3S_8$ exhibits paramagnetic behavior at $T > 150$ K (Figure 4e). A Curie–Weiss law fit of $T > 275$ K gives a Curie constant of 1.871(2) K mol^{-1} Oe^{1-}, Weiss temperature 6.5(4) K, and p_{eff} = 3.898(7) μ_B. The determined effective magnetic moment for $Li_2CoSn_3S_8$ is close to the theoretical value of 3.87 μ_B expected for Co^{2+}.[61] The positive Weiss temperature suggests ferromagnetic interactions, which is consistent with a paramagnetic to ferromagnetic phase transition observed having approximate T_c = ∼121 K. Field-dependent measurements were performed both below and above the apparent ferromagnetic transition at T = 2 and 130 K to further study the ferromagnetic behavior, as shown in Figure 4f. Hysteresis is observed at 2 K with a coercivity of ∼27 Oe, indicating a soft ferromagnetic character. At 130 K, the response to the applied field is almost linear, indicating that we are above but still near the T_c of $Li_2CoSn_3S_8$.

Electrical Resistivity and Impedance Spectroscopy. The electrical resistivities of all the compounds fall between 2.38×10^3 and 2.9×10^7 Ω-cm, as shown in Table 5. The most resistive compound is $Li_2MgSn_3S_8$ because of its larger band gap. $Li_2NiSn_3S_8$, $Li_2MnSn_3S_8$, and $Li_{1.66}CuSn_{3.33}S_8$ all have resistivities on the order of 10^6 Ω-cm and follow the trend of decreasing band gap as they are ordered from smallest to largest. The two most conductive compounds are $Li_2CoSn_3S_8$ and $Li_2FeSn_3S_8$ with resistivities of 3.47×10^4 and 2.8×10^3 Ω-cm, respectively. The resistivity of $Li_2FeSn_3S_8$ was comparable to that of $A_2FeSn_3S_8$ (A = Ag, Cu).[53]

The conductivities determined using AC impedance spectroscopy for $Li_2FeSn_3S_8$ and $Li_2CoSn_3S_8$, 1.9×10^{-4} and 1.11×10^{-3} S cm^{-1}, respectively, are notably high and most likely

https://dx.doi.org/10.1021/acs.chemmater.0c04651
Chem. Mater. 2021, 33, 2080–2089

capture contributions from electronic conduction, see Figure 5e and c. The Li-ion conductivities of $Li_2MgSn_3S_8$, $Li_2MnSn_3S_8$, $Li_2NiSn_3S_8$, and $Li_{1.66}CuSn_{3.33}S_8$, Figure 5a, b, d, and f, are determined to be 1.26×10^{-7}, 1.94×10^{-7}, 1.93×10^{-6}, and 2.55×10^{-9} S cm^{-1}, respectively. The low Li-ion conductivities, suggesting limited probability of Li migration, are consistent with the apparent moisture resistance of the compounds, as the Li^+ ions are well coordinated in the lattice and so cannot migrate. This lack of mobility limits the rate of decomposition of this family of compounds.

CONCLUSIONS

Seven new air-stable isostructural quaternary Li-containing 3D thiostannate spinels with semiconducting properties were synthesized. The origin of their stability in air and moisture is attributed to the Li^+ being well-coordinated inside the structure and, thus, largely shielded from attack. Their structures are to be contrasted with the layered ones of the KMS family of compounds with similar stoichiometry but larger alkali ions. The higher dimensionality, as expressed by the 3D cubic motif, of the lithium salts than the corresponding heavier alkali metal thiostannates, is well rationalized by the so-called counterion effect observed in other metal chalcogenide salts.[57] These results highlight a general approach for targeting the dimensionality of solids using counterion size as the controlling parameter.[57] The large exploratory phase space that exists for small cation chalcogenides thus presents an exciting opportunity to study the role of small cations in controlling dimensionality in these materials. The moisture resistance of these compounds implies a lower lithium translational mobility compared to other chalcogenides, which decompose readily in air.

ASSOCIATED CONTENT

Supporting Information

The Supporting Information is available free of charge at https://pubs.acs.org/doi/10.1021/acs.chemmater.0c04651.

Synthetic procedures for the preparation of $Li_2MSn_3S_8$ (M = Co, Mn, Fe, Ni) and $Li_{1.66}CuSn_{3.33}S_8$, as well as the methods used to collect powder X-ray diffraction, single-crystal diffraction, differential thermal analysis, and UV−vis diffuse reflectance (PDF)

Crystallographic information file for $Li_{1.66}CuSn_{3.33}S_8$ (CIF)

Crystallographic information file for $Li_2CoSn_3S_8$ (CIF)

Crystallographic information file for $Li_2FeSn_3S_8$ (CIF)

Crystallographic information file for $Li_2MgSn_3S_8$ (CIF)

Crystallographic information file for $Li_2MnSn_3S_8$ (CIF)

Crystallographic information file for $Li_2NiSn_3S_8$ (CIF)

Optimized coordinates for $Li_{1.66}CuSn_{3.33}S_8$ (TXT)

Optimized coordinates for $Li_2MgSn_3S_8$ (TXT)

AUTHOR INFORMATION

Corresponding Author

Mercouri G. Kanatzidis − *Department of Chemistry, Northwestern University, Evanston, Illinois 60208, United States;* orcid.org/0000-0003-2037-4168; Email: m-kanatzidis@northwestern.edu

Authors

Michael A. Quintero − *Department of Chemistry, Northwestern University, Evanston, Illinois 60208, United States;* orcid.org/0000-0002-0709-1676

Shiqiang Hao − *Department of Materials Science and Engineering, Northwestern University, Evanston, Illinois 60208, United States;* orcid.org/0000-0002-7985-4468

Sawankumar V. Patel − *Department of Chemistry & Biochemistry, Florida State University, Tallahassee, Florida 30206, United States;* orcid.org/0000-0002-5293-9330

Jin-Ke Bao − *Materials Science Division, Argonne National Laboratory, Lemont, Illinois 60439, United States;* orcid.org/0000-0001-5522-3605

Xiuquan Zhou − *Materials Science Division, Argonne National Laboratory, Lemont, Illinois 60439, United States;* orcid.org/0000-0002-1361-3880

Yan-Yan Hu − *Department of Chemistry & Biochemistry, Florida State University, Tallahassee, Florida 30206, United States; Center of Interdisciplinary Magnetic Resonance, National High Magnetic Field Laboratory, Tallahassee, Florida 32310, United States;* orcid.org/0000-0003-0677-5897

Chris Wolverton − *Department of Materials Science and Engineering, Northwestern University, Evanston, Illinois 60208, United States;* orcid.org/0000-0003-2248-474X

Complete contact information is available at: https://pubs.acs.org/10.1021/acs.chemmater.0c04651

Notes

The authors declare no competing financial interest.

ACKNOWLEDGMENTS

The synthesis and materials characterization work was supported by the National Science Foundation through Grant DMR-2003476. The magnetic susceptibility measurements were supported by Laboratory Directed Research and Development (LDRD) funding from Argonne National Laboratory, provided by the Director, Office of Science of the US Department of Energy under contract number DEAC02-06CH11357. This work made use of the SPID and EPIC facilities of Northwestern University's NUANCE Center, which has received support from the Soft and Hybrid Nanotechnology Experimental (SHyNE) Resource (NSF ECCS-1542205); the MRSEC program (NSF DMR-1720139) at the Materials Research Center; the International Institute for Nanotechnology (IIN); the Keck Foundation; and the State of Illinois, through IIN. This work made use of IMSERC at Northwestern University, which has received support from the Soft and Hybrid Nanotechnology Experimental (SHyNE) Resource (NSF ECCS-1542205), the State of Illinois and IIN. This work made use of the EPIC facility of Northwestern University's NUANCE Center, which has received support from the SHyNE Resource (NSF ECCS-2025633), the IIN, and Northwestern's MRSEC program (NSF DMR-1720139).

REFERENCES

(1) Hill, R. J.; Craig, J. R.; Gibbs, G. Systematics of the spinel structure type. *Phys. Chem. Miner.* **1979**, *4* (4), 317−339.

(2) Pinch, H.; Woods, M.; Lopatin, E. Some new mixed A-site chromium chalcogenide spinels. *Mater. Res. Bull.* **1970**, *5* (6), 425−429.

(3) Harada, S. Some new sulfo-spinels containing iron-group transition metals. *Mater. Res. Bull.* **1973**, *8* (12), 1361−1369.
(4) Abou Ghaloun, O.; Chevalier, P.; Trichet, L.; Rouxel, J. Lithium Yttrium Zirconium Sulfide (LIXYXZR1-XS2) Ionic Conductors. *Rev. Chim. Mineral.* **1980**, *17*, 368.
(5) Yohannan, J. P.; Vidyasagar, K. Syntheses, structural variants and characterization of AInM' S4 (A= alkali metals, Tl; M'= Ge, Sn) compounds; facile ion-exchange reactions of layered NaInSnS4 and KInSnS4 compounds. *J. Solid State Chem.* **2016**, *238*, 291−302.
(6) Kanno, R.; Takeda, Y.; Yamamoto, O. Structure, ionic conductivity and phase transformation of double chloride spinels. *Solid State Ionics* **1988**, *28*, 1276−1281.
(7) Haussühl, S. Anomalous thermoelastic properties of the cyanospinels K2Zn (CN) 4, K2Cd (CN) 4 and K2Hg (CN) 4. *Acta Crystallogr., Sect. A: Cryst. Phys., Diffr., Theor. Gen. Crystallogr.* **1976**, *32* (1), 160−162.
(8) Hashikuni, K.; Suekuni, K.; Usui, H.; Chetty, R.; Ohta, M.; Kuroki, K.; Takabatake, T.; Watanabe, K.; Ohtaki, M. Thermoelectric Properties and Electronic Structures of CuTi2S4 Thiospinel and Its Derivatives: Structural Design for Spinel-Related Thermoelectric Materials. *Inorg. Chem.* **2019**, *58* (2), 1425−1432.
(9) Hashikuni, K.; Suekuni, K.; Watanabe, K.; Bouyrie, Y.; Ohta, M.; Ohtaki, M.; Takabatake, T. Carrier concentration tuning in thermoelectric thiospinel Cu2CoTi3S8 by oxidative extraction of copper. *J. Solid State Chem.* **2018**, *259*, 5−10.
(10) Tewari, G. C.; Tripathi, T.; Rastogi, A. Thermoelectric Properties of Layer-Antiferromagnet CuCrS 2. *J. Electron. Mater.* **2010**, *39* (8), 1133−1139.
(11) Sharma, R.; Dwivedi, S.; Sharma, Y. Transport Properties in Thiospinel ZnX2S4 (X= Al, Ga, In) as Promising Thermoelectric Materials. *Adv. Sci. Lett.* **2016**, *22* (11), 3840−3843.
(12) Sun, X.; Bonnick, P.; Duffort, V.; Liu, M.; Rong, Z.; Persson, K. A.; Ceder, G.; Nazar, L. F. A high capacity thiospinel cathode for Mg batteries. *Energy Environ. Sci.* **2016**, *9* (7), 2273−2277.
(13) Canepa, P.; Bo, S.-H.; Sai Gautam, G.; Key, B.; Richards, W. D.; Shi, T.; Tian, Y.; Wang, Y.; Li, J.; Ceder, G. High magnesium mobility in ternary spinel chalcogenides. *Nat. Commun.* **2017**, *8* (1), 1759.
(14) Wustrow, A.; Key, B.; Phillips, P. J.; Sa, N.; Lipton, A. S.; Klie, R. F.; Vaughey, J. T.; Poeppelmeier, K. R. Synthesis and Characterization of MgCr2S4 Thiospinel as a Potential Magnesium Cathode. *Inorg. Chem.* **2018**, *57* (14), 8634−8638.
(15) Furubayashi, T.; Matsumoto, T.; Hagino, T.; Nagata, S. Structural and magnetic studies of metal-insulator transition in thiospinel CuIr2S4. *J. Phys. Soc. Jpn.* **1994**, *63* (9), 3333−3339.
(16) Fichtl, R.; Tsurkan, V.; Lunkenheimer, P.; Hemberger, J.; Fritsch, V.; von Nidda, H.-A. K.; Scheidt, E.-W.; Loidl, A. Orbital Freezing and Orbital Glass State in F e C r 2 S 4. *Phys. Rev. Lett.* **2005**, *94* (2), 027601.
(17) Hagino, T.; Seki, Y.; Wada, N.; Tsuji, S.; Shirane, T.; Kumagai, K.-i.; Nagata, S. Superconductivity in spinel-type compounds CuRh 2 S 4 and CuRh 2 Se 4. *Phys. Rev. B: Condens. Matter Mater. Phys.* **1995**, *51* (18), 12673.
(18) Ohno, S.; Helm, B.; Fuchs, T.; Dewald, G.; Kraft, M. A.; Culver, S. P.; Senyshyn, A.; Zeier, W. G. Further Evidence for Energy Landscape Flattening in the Superionic Argyrodites Li6+ x P1-x M x S5I (M= Si, Ge, Sn). *Chem. Mater.* **2019**, *31* (13), 4936−4944.
(19) Minafra, N.; Culver, S. P.; Krauskopf, T.; Senyshyn, A.; Zeier, W. G. Effect of Si substitution on the structural and transport properties of superionic Li-argyrodites. *J. Mater. Chem. A* **2018**, *6* (2), 645−651.
(20) Kong, S. T.; Deiseroth, H. J.; Reiner, C.; Gün, Ö.; Neumann, E.; Ritter, C.; Zahn, D. Lithium argyrodites with phosphorus and arsenic: order and disorder of lithium atoms, crystal chemistry, and phase transitions. *Chem. - Eur. J.* **2010**, *16* (7), 2198−2206.
(21) Kanno, R.; Murayama, M. Lithium ionic conductor thio-LISICON: the Li2 S GeS2 P 2 S 5 system. *J. Electrochem. Soc.* **2001**, *148* (7), A742.
(22) Inoue, Y.; Suzuki, K.; Matsui, N.; Hirayama, M.; Kanno, R. Synthesis and structure of novel lithium-ion conductor Li7Ge3PS12. *J. Solid State Chem.* **2017**, *246*, 334−340.
(23) Bera, T. K.; Kanatzidis, M. G. AEuAsS3 (A= Li, K, Rb, and Cs): new As3+ species from an arsenic-rich polysulfide flux. *Inorg. Chem.* **2008**, *47* (16), 7068−7070.
(24) Brant, J. A.; dela Cruz, C.; Yao, J.; Douvalis, A. P.; Bakas, T.; Sorescu, M.; Aitken, J. A. Field-Induced Spin-Flop in Antiferromagnetic Semiconductors with Commensurate and Incommensurate Magnetic Structures: Li2FeGeS4 (LIGS) and Li2FeSnS4 (LITS). *Inorg. Chem.* **2014**, *53* (23), 12265−12274.
(25) Mei, D.; Zhang, S.; Liang, F.; Zhao, S.; Jiang, J.; Zhong, J.; Lin, Z.; Wu, Y. LiGaGe2S6: a chalcogenide with good infrared nonlinear optical performance and low melting point. *Inorg. Chem.* **2017**, *56* (21), 13267−13273.
(26) Yin, W.; Feng, K.; Mei, D.; Yao, J.; Fu, P.; Wu, Y. Ba 2 AgInS 4 and Ba 4 MGa 5 Se 12 (M= Ag, Li): syntheses, structures, and optical properties. *Dalton Transactions* **2012**, *41* (8), 2272−2276.
(27) Chica, D. G.; He, Y.; McCall, K. M.; Chung, D. Y.; Pak, R. O.; Trimarchi, G.; Liu, Z.; De Lurgio, P. M.; Wessels, B. W.; Kanatzidis, M. G. Direct thermal neutron detection by the 2D semiconductor 6 LiInP 2 Se 6. *Nature* **2020**, *577* (7790), 346−349.
(28) Bron, P.; Johansson, S.; Zick, K.; Schmedt auf der Günne, J. r.; Dehnen, S.; Roling, B. Li10SnP2S12: an affordable lithium superionic conductor. *J. Am. Chem. Soc.* **2013**, *135* (42), 15694−15697.
(29) Kato, Y.; Hori, S.; Saito, T.; Suzuki, K.; Hirayama, M.; Mitsui, A.; Yonemura, M.; Iba, H.; Kanno, R. High-power all-solid-state batteries using sulfide superionic conductors. *Nature Energy* **2016**, *1* (4), 16030.
(30) Lu, Y.-J.; Ibers, J. A. Alkali-Metal Substitution into Solid-State Chalcogenides: Effects on Dimensionality. *Comments Inorg. Chem.* **1993**, *14* (4), 229−243.
(31) Long, J. R.; McCarty, L. S.; Holm, R. A solid-state route to molecular clusters: Access to the solution chemistry of [Re6Q8] 2+(Q= S, Se) core-containing clusters via dimensional reduction. *J. Am. Chem. Soc.* **1996**, *118* (19), 4603−4616.
(32) Axtell, E. A.; Park, Y.; Chondroudis, K.; Kanatzidis, M. G. Incorporation of A2Q into HgQ and dimensional reduction to A2Hg3Q4 and A2Hg6Q7 (A= K, Rb, Cs; Q= S, Se). Access of Li ions in A2Hg6Q7 through topotactic ion-exchange. *J. Am. Chem. Soc.* **1998**, *120* (1), 124−136.
(33) Axtell III, E. A.; Liao, J. H.; Pikramenou, Z.; Kanatzidis, M. G. Dimensional reduction in II-VI materials: A2Cd3Q4 (A= K, Q= S, Se, Te; A= Rb, Q= S, Se), novel ternary low-dimensional cadmium chalcogenides produced by incorporation of A2Q in CdQ. *Chem. - Eur. J.* **1996**, *2* (6), 656−666.
(34) Tulsky, E. G.; Long, J. R. Dimensional reduction: a practical formalism for manipulating solid structures. *Chem. Mater.* **2001**, *13* (4), 1149−1166.
(35) Androulakis, J.; Peter, S. C.; Li, H.; Malliakas, C. D.; Peters, J. A.; Liu, Z.; Wessels, B. W.; Song, J. H.; Jin, H.; Freeman, A. J.; et al. Dimensional reduction: a design tool for new radiation detection materials. *Adv. Mater.* **2011**, *23* (36), 4163−4167.
(36) Brunn, H.; Hoppe, R. Neue ternäre Oxide der Seltenen Erden: Über RbSEO 2 (SE= La, Nd, Sm, Eu, Gd) sowie CsNdO2 [1, 2]. *Z. Anorg. Allg. Chem.* **1975**, *417* (3), 213−220.
(37) Wiench, H.; Brachtel, G.; Hoppe, R. Die Kristallstruktur von?? RbScO2. *Z. Anorg. Allg. Chem.* **1977**, *436* (1), 169−172.
(38) Roth, H. F.; Meyer, G.; Hu, Z.; Kaindl, G. Synthesis, structure, and X-ray absorption spectra of LixNbO2 and NaxNbO2 (x≤ 1). *Z. Anorg. Allg. Chem.* **1993**, *619* (8), 1369−1373.
(39) Meyer, G.; Hoppe, R. Über Oxoniobate (III): zur kenntnis von LiNbO2. *J. Less-Common Met.* **1976**, *46* (1), 55−65.
(40) Mertz, J. L.; Fard, Z. H.; Malliakas, C. D.; Manos, M. J.; Kanatzidis, M. G. Selective Removal of Cs+, Sr2+, and Ni2+ by K2 x Mg x Sn3-x S6 (x= 0.5−1)(KMS-2) Relevant to Nuclear Waste Remediation. *Chem. Mater.* **2013**, *25* (10), 2116−2127.

(41) Manos, M. J.; Kanatzidis, M. G. Highly Efficient and Rapid Cs+ Uptake by the Layered Metal Sulfide K2 x Mn x Sn3- x S6 (KMS-1). *J. Am. Chem. Soc.* **2009**, *131* (18), 6599−6607.
(42) Xiao, C.; Hassanzadeh Fard, Z.; Sarma, D.; Song, T.-B.; Xu, C.; Kanatzidis, M. G. Highly efficient separation of trivalent minor actinides by a layered metal sulfide (KInSn2S6) from acidic radioactive waste. *J. Am. Chem. Soc.* **2017**, *139* (46), 16494−16497.
(43) Khoury, J. F.; Hao, S.; Stoumpos, C. C.; Yao, Z.; Malliakas, C. D.; Aydemir, U.; Slade, T. J.; Snyder, G. J.; Wolverton, C.; Kanatzidis, M. G. Quaternary Pavonites A1+ x Sn2-x Bi5+ x S10 (A+= Li+, Na+): Site Occupancy Disorder Defines Electronic Structure. *Inorg. Chem.* **2018**, *57* (4), 2260−2268.
(44) Perdew, J. P.; Burke, K.; Ernzerhof, M. Generalized gradient approximation made simple. *Phys. Rev. Lett.* **1996**, *77* (18), 3865.
(45) Kresse, G.; Furthmüller, J. Efficient iterative schemes for ab initio total-energy calculations using a plane-wave basis set. *Phys. Rev. B: Condens. Matter Mater. Phys.* **1996**, *54* (16), 11169.
(46) West, A. R. *Solid State Chemistry and Its Applications*; John Wiley & Sons, 2014; pp 187−228.
(47) Knauth, P. Inorganic solid Li ion conductors: An overview. *Solid State Ionics* **2009**, *180* (14−16), 911−916.
(48) Guerard, D.; Herold, A. Intercalation of lithium into graphite and other carbons. *Carbon* **1975**, *13* (4), 337−345.
(49) Hazen, R. M.; Finger, L. W. The crystal structures and compressibilities of layer minerals at high pressure; I, SnS < 2, berndtite. *Am. Mineral.* **1978**, *63* (3−4), 289−292.
(50) Lavela, P.; Tirado, J. L.; Morales, J.; Olivier-Fourcade, J.; Jumas, J.-C. Lithium intercalation and copper extraction in spinel sulfides of general formula Cu 2 MSn 3 S 8 (M= Mn, Fe, Co, Ni). *J. Mater. Chem.* **1996**, *6* (1), 41−47.
(51) Shannon, R. D. Revised effective ionic radii and systematic studies of interatomic distances in halides and chalcogenides. *Acta Crystallogr., Sect. A: Cryst. Phys., Diffr., Theor. Gen. Crystallogr.* **1976**, *32* (5), 751−767.
(52) Garg, G.; Ramanujachary, K.; Lofland, S.; Lobanov, M.; Greenblatt, M.; Maddanimath, T.; Vijayamohanan, K.; Ganguli, A. Crystal structure, magnetic and electrochemical properties of a quaternary thiospinel: Ag2MnSn3S8. *J. Solid State Chem.* **2003**, *174* (1), 229−232.
(53) Garg, G.; Gupta, S.; Maddanimath, T.; Gascoin, F.; Ganguli, A. K. Single crystal structure, electrical and electrochemical properties of the quaternary thiospinel: Ag2FeSn3S8. *Solid State Ionics* **2003**, *164* (3−4), 205−209.
(54) Aitken, J. A.; Chondroudis, K.; Young, V. G., Jr.; Kanatzidis, M. G. LiEuPSe4 and KEuPSe4: Novel selenophosphates with the tetrahedral [PSe4] 3-building block. *Inorg. Chem.* **2000**, *39* (7), 1525−1533.
(55) Kim, J.; Wang, C.; Hughbanks, T. Synthesis and Structures of New Layered Ternary Manganese Tellurides: AMnTe2 (A= Li, Na). *Inorg. Chem.* **1998**, *37* (7), 1428−1429.
(56) Kim, J.; Hughbanks, T. Synthesis and structures of new ternary aluminum chalcogenides: LiAlSe2, α-LiAlTe2, and β-LiAlTe2. *Inorg. Chem.* **2000**, *39* (14), 3092−3097.
(57) Kanatzidis, M. G. Counterion size versus structure in metal-chalcogenide salts. *Phosphorus, Sulfur Silicon Relat. Elem.* **1994**, *93* (1−4), 159−172.
(58) DiMasi, E.; Aronson, M.; Mansfield, J.; Foran, B.; Lee, S. Chemical pressure and charge-density waves in rare-earth tritellurides. *Phys. Rev. B: Condens. Matter Mater. Phys.* **1995**, *52* (20), 14516.
(59) Fredrickson, D. C. Electronic Packing Frustration in Complex Intermetallic Structures: The Role of Chemical Pressure in Ca2Ag7. *J. Am. Chem. Soc.* **2011**, *133* (26), 10070−10073.
(60) Zunger, A. *Beware of Plausible Predictions of Fantasy Materials*. Nature Publishing Group, 2019; pp 447−449.
(61) Ashcroft, N. W.; Mermin, N. D. *Solid State Physics*; Neil, W. A., Mermin, N. D., Eds.; Holt, Rinehart, and Winston: New York, 1976; p 658.
(62) Azzoni, C.; Mozzati, M.; Paleari, A.; Massarotti, V.; Bini, M.; Capsoni, D. Evidence of a cationic substitution domain in lithium-manganese spinels. *Z. Naturforsch., A: Phys. Sci.* **1998**, *53* (9), 771−778.

https://dx.doi.org/10.1021/acs.chemmater.0c04651
Chem. Mater. 2021, 33, 2080−2089